

Local-global method to predict distortion of aircraft panel caused in automated riveting process

Di Yang, Weiwei Qu and Yinglin Ke
Zhejiang University, Hangzhou, China

Abstract

Purpose – The riveting process is a metal forming process involving complex elastic-plastic deformation, which will induce a compressive residual stress field and cause local distortions in the connecting areas. Regarding to the aircraft panel assemblies with plenty of rivets, the global deformation is inevitable and undesired, leading difficulties to downstream assembly processes. This paper aims to present a new method for the local distortion calculation and the global deformation prediction of sheet panel assemblies during the automated riveting process.

Design/methodology/approach – In this paper, a simplified algebraic study is presented to analyze the local distortion of single countersunk rivet joint with the consideration of the barrel-like shape of the driven head and the through-thickness variations along the rivet shank. Then, an equivalent rivet unit is proposed based on the result of the algebraic study and embedded into the global-level model for the prediction of the overall distortions of riveted panels.

Findings – The algebraic study is able to reach a more precise contour of the deformed rivet than the traditional assumption of cylindrical deformations and rapidly determine the equivalent coefficients of the riveting unit. The result also shows an industrial acceptable accuracy of the prediction for the global deformations of the double-layered panel assemblies widely used in the aircraft panel structures.

Originality/value – A new local-global method for predicting the deformations of the riveted panel assembly based on the algebraic study of the local distortions is proposed to help the engineers in the early design stages or in the assembly process planning stage.

Keywords Automatic riveting, Local-global method, Riveting assembly deformation, Simplified model

Paper type Research paper

1. Introduction

Riveting joints of aluminum-alloy sheet material are extensively adopted in the aircraft structure designs. The riveting process creates a pattern of circumferential compressive stress for the improvement of the fatigue life of the local assembled joints. However, a lone line of such stress patterns usually causes the dimensional growth of the assembly, primarily in the longitudinal direction, and can cause an elongated part to deflect along its length (Munk *et al.*, 2004). For large-scaled assemblies with numerous rivets, this undesired distortion will finally lead to difficulties in the downstream manufacturing process, like making the assembly of two fuselage cross-sections infeasible on originally planned time. Attempts to restrain these accumulated distortions for large-scaled assemblies are usually fruitless. So, the most effective approach to date has been to attempt to predict the extend of the distortion and account for it in the original design of the parts, or in the assembly process planning stage with the intent that the assembly will distort to a shape that is approximately what is called for in the design.

As the riveting process is quite complicated due to large displacement effect, contact phenomenon and material

nonlinearity (Aman *et al.*, 2013), it is not practical to construct and simulate detailed models for large assemblies. Some simplifications have been brought in to the studies in modeling the aircraft assembly variations involving the rivet joints. Liu *et al.* (2014a, 2014b) proposed key features based on MIC methods for the variation analysis of fuselage panel riveting assembly. In this method, the local elastic-plastic deformation near the hole wall was ignored, and the global variation caused by riveting is simplified as being caused by bending moments. Cheng *et al.* (2011, 2012) proposed a variation propagation model for aeronautical thin-walled structures (ATWSs) with multi-state riveting. In this model, the riveting state was derived from the pre-joining state by calculating the riveting variation as a vector superposition of the gap-closing effect and the undetermined plastic deformation. Saadat and Cretin (2002) Saadat *et al.* (2007) described a methodology to predict overall deformation between the alignment of the rib foot and the skin panel. The assembly operations were conducted under simulated laboratory conditions by certain load units, while the simulation study was conducted positional displacements of

The current issue and full text archive of this journal is available on Emerald Insight at: www.emeraldinsight.com/0144-5154.htm



Assembly Automation
39/5 (2019) 973–985
© Emerald Publishing Limited [ISSN 0144-5154]
[DOI 10.1108/AA-06-2018-079]

This research was supported by the Science Fund for Creative Research Groups of National Natural Science Foundation of China (No.: 51221004, 51821093) and the National Natural Science Foundation of China (51521064).

Received 8 June 2018
Revised 25 January 2019
7 April 2019
15 May 2019
Accepted 30 May 2019

relevant rib feet. Lin *et al.* (2014) proposed an efficient deviation propagation model (DPM) based on substructures to reduce the complexity. In this method, finite element (FE) models with compliant parts were condensed into substructures with fewer degrees of freedoms (DOFs), and the riveting fasteners were condensed to coupled key features with relevant DOF tied together. All these studies had made suitable simplification in different complexity level to cooperate with their research objects. Yet they still tended to oversimplify the description of the complex mechanical behavior of the local riveting joints.

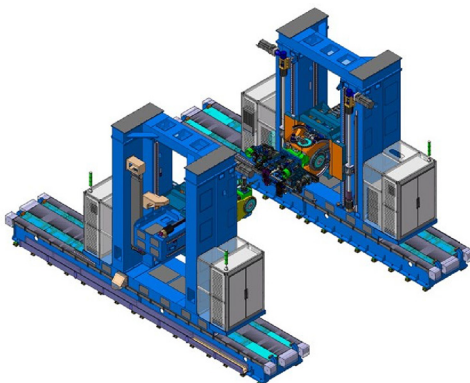
For now, automated riveting machines are widely used in the aircraft industry. Figure 1 shows an automated riveting machine independently developed. In contrast with the traditional manual operations, the automated riveting process excludes the randomness induced by human factors. Hence, it is possible to analyze the local distortion pattern of single rivet first and mapping it into the global level model for the overall distortion prediction. In the context of local distortion and residual stress field study, many scholars have done a lot of basic works. Li *et al.* (2006a, 2006b) used both experiments and FE simulations to study the single-row countersunk riveted lap joints. The results showed that with proper boundary conditions, the FE modeling could reliably be used to determine the residual stress/strain during the riveting process. Langrand *et al.* (2002a, 2002b) dealt with experimental works aiming at improving the design of riveted joints for airframe crashworthiness purposes. Complex assemblies were considered as the sum of simpler ones constituted of one rivet and two plates, the behavior of which was investigated through experimental works parallel with numerical simulations. Blanchot and Daidie (2006) presented the simulation of riveting process and its influence on the riveted link behavior. They developed three different FE models for the axial and radial tests, the slice, axisymmetric and symmetric model. Derijck *et al.* (2007) investigated the relation between the squeeze load F_{sq} and the rivet head dimensions during controlled squeezing. Manes *et al.* (2011) studied the effect of the riveting parameters on the stress field close to the holes of T-cleats used in helicopter fuselage panels. A detailed FE model including two sub-models with particular attention paid to the simulation of the rivet forming had been developed and experimentally validated. Cheraghi (2008) presented a study

on the effect of some controllable process parameters in riveting. A good combination of riveting process parameters was found to minimize the residual stress in sheets and rivets, bulging and material growth in sheets. All these studies have provided good references for the understanding of the local riveting process.

The riveting-induced distortions are still understudied in academics. Based on the idea of local-global concept, some researches have been conducted for evaluating the consequent global distortions with the understanding of the local joint behavior. Eckert *et al.* (2013) studied the result quality of 2D rotational simulations of single self-piercing rivet (SPR), and the usage of a local simplified model for the joining operation to prediction of the global dimensional accuracy of a car body assembly. The local model was implemented into the global-level part FE model through applying the distortion causing loads in the area around the linked sheets. Ni *et al.* (2016) proposed a local-to-global FE analyses framework for the dimensional analysis of large-scale antennas. The framework was made up of a number of static FE analysis taking into account the inherent strain data of the local riveting process, which was extracted as the coordinates and displacements of the nodes around the part hole. Wang (2014) presented the method of riveting sequence optimization with the consideration of the final distortions of a horizontal stabilizer. Based on the local riveting analysis, he employed the principal stress method to calculate the lateral force induced by the metal flow during single riveting, and the equivalent loads were applied to the hole surfaces in the global-level FE model as a pressure in the inner riveting holes, neglecting the interference variation through thickness. Based on Wang's study, Chang *et al.* (2016) proposed a successive calculation model to study the riveting deformation using FEM with the consideration of local deformation and riveting sequence. Kaniowski *et al.* (2009) dealt with the modeling of riveted joints in aircraft structures with FE methods in three different complexity levels, namely, considering the complete structure, a structural detail and a single riveted joint. On the basis of the result of single rivet joint, a method of modeling local residual stresses with temperature and thermal coefficient was used. Figueira and Trabasso (2015) proposed a simplified algebraic modeling for the riveting line expansion calculation as the accumulation of single rivet distortions. The local analysis was based on the rivet's and hole wall's mutual interactions along the rivet squeezing, under the cylindrical shape assumption. Abdelal *et al.* (2015) presented a study on the deformation of small panel assemblies with multiple rivets through both simplified static stress FE model and explicit FE model. The local static stress was modeled by an expansible rivet simulating the real rivet deformation.

So far, most of the researches (Wang, 2014; Chang *et al.*, 2016; Figueira and Trabasso, 2015) have dealt with the assumption that only diameters and lengths of the rivet change, but the cylindrical shape of both the driven head and the shank do not change. However, in the aircraft panel assembly, large-scaled skin-stringer panels of wings and fuselages are always automated riveted by countersunk head rivets due to the requirement of the aerodynamic performance. Different from the protruding head rivets, the compressive stress through the sheet thickness is quite non-uniform and is a main cause to the

Figure 1 An automated riveting machine



deflection of the riveted structures. Hence, the through-thickness variation of the rivet shank and the correlative deformation of the barrel-like shape-driven head need to be considered. In the global-level modeling, previous researches (Eckert *et al.*, 2013; Ni *et al.*, 2016; Wang, 2014; Chang *et al.*, 2016) implemented the local distortions by directly applying the equivalent pressure or displacement field to the hole surfaces or the relevant FE nodes, which is named as the equivalent load method. Kaniowski *et al.* (2009) and Abdelal *et al.* (2015) used simplified expansible rivet units to simulating the real rivet deformations. Both methods are focused on the final distortions at the interfaces of the riveted hole and the rivet shank. In this research, we proposed an equivalent unit method for simulating the radial expansion in the elastic region at the vicinity of riveted hole. Through the analytical analysis and neglecting the plastic region in the global-level model, the method is considered having the capability of quick calculation and modeling in the design and process planning states for the global distortion prediction of riveted structures.

In the first part of Section 2, a simplified analytical study is presented to analyze the local distortion of single countersunk rivet joint with the consideration of the barrel-like shape of the driven head and the through-thickness variations along the rivet shank. In the second part of Section 2, an equivalent rivet unit is proposed based on the result of the analytical study and embedded into the global-level model for the prediction of the overall distortions of riveted sheets. In Section 3, the simulation and experimental tests are carried out for the validations of both the single rivet distortions and the multiple rivets deformations. Conclusions are drawn in Section 4.

2. Methodology

2.1 Analytical study on distortion of single countersunk rivet

2.1.1 Riveting process and the volume consistency

Figure 2 shows the initial state of a double-layer lap joint with a countersunk rivet. The rivet is assumed on a large enough panels with stress-free boundary conditions. The rivet consists of a cylindric body and a cone shape head and is inserted through the countersunk hole from the outer sheet side. The dimension symbols are list in Table I. The origin volume of the

Figure 2 Riveting process of a typical countersunk rivet joint

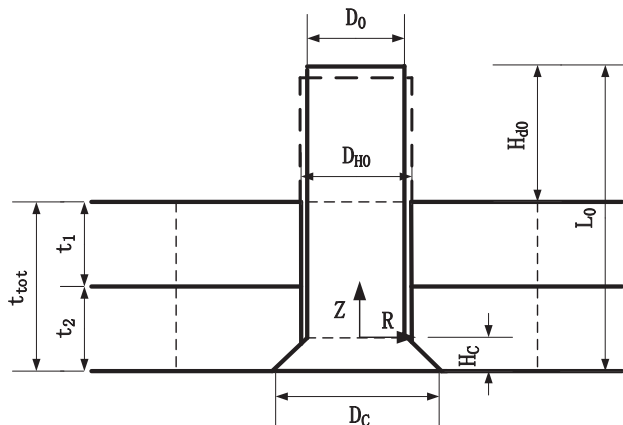


Table I Symbol definition of the riveting geometries

Symbol	Definition
t_1, t_2	Thickness of two sheets
t_{tot}	Total thickness of two layers
D_0	Original shank diameter
D_{HO}	Original hole diameter
H_c	Depth of countersunk of hole
L_0	Length of origin rivet
H_{40}	Height of driven head part
D_c	Diameter of countersunk head
$D(z)$	Diameter of driven head
H	Height of driven head
L_t	Length of deformed rivet
H_s	Height of Shank
$d(z)$	Diameter of riveted shank

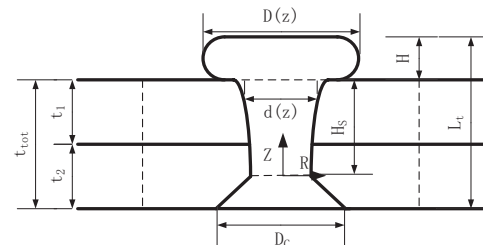
rivet can be calculated as the summation of the countersunk head and rivet shank:

$$V_0 = \frac{1}{3} \pi H_c \left(\frac{D_c^2}{4} + \frac{D_0^2}{4} + \frac{D_c D_0}{4} \right) + \frac{1}{4} \pi D_0^2 (L_0 - H_c) \quad (1)$$

The upper riveting head contacts and sustains the countersunk side, than the lower riveting head begins riveting. After the squeezing force F_{sq} is applied to the tail of the rivet shank by the punch, the rivet shank is assumed to expand uniformly till it contact the hole wall as shown by dashed line in Figure 2. At this moment, the diameter of the rivet is D_{HO} . Afterwards, the portion outside the hole initiate the formation of the driven head, and a fraction of the head material flows into the hole. From this moment on, along with the squeezing force continuously applied to the rivet, the rivet shank expands and starts to extrude the material at inner surfaces of the hole, and the driven head keeps shaping. The material at the hole vicinity quickly arrived at its yield limit, and the plastic deformations occur until the driven head reached its final height H , which is usually used as the control factor in the automated riveting process.

As a small portion of the driven head has been gradually inserted into the hole, and the diameter at the countersunk end is barely not expanded, the interferences are varied through thickness. As shown in Figure 3, the diameter at the driven head side is slightly larger than the one at the countersunk head. The final volume of the rivet can be expressed as the

Figure 3 The formation of the countersunk rivet



summation of the driven head, the rivet shank and the countersunk head:

$$V_t = V_{Ht} + V_{St} + V_{Ct}$$

$$= \int_0^H \frac{\pi}{4} D^2(z) dz + \int_0^{H_s} \frac{\pi}{4} d^2(z) dz$$

$$+ \frac{1}{3} \pi H_C \left(\frac{D_C^2}{4} + \frac{d_S^2(0)}{4} + \frac{D_C d_S(0)}{4} \right) \quad (2)$$

A calculation of the volume of the rivet after squeezing confirmed that the volume of the rivet after squeezing remained accurately constant if the small volume contribution due to the small hole expansion is taken into account (Derijck *et al.*, 2007). Hence, the volume of the rivet is considered invariable along the riveting process:

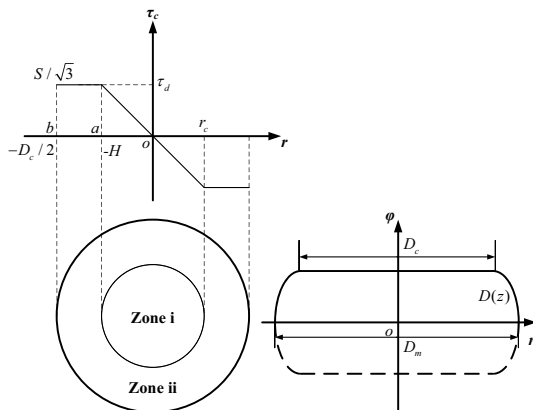
$$V_0 = V_t \quad (3)$$

2.1.2 Shape modelling of the driven head

Large plastic strains occur in the material of the driven head during the squeezing process. Excluding a small portion of material flowed into the hole, the rivet shank outsider the hole area deforms with the constrain between the upper surface of the inner sheet and the riveting die. The elastic strains are ignored because they are very small compared to the plastic strains.

Due to the influence of the friction, the driven head always forms a barrel-like shape rather than a cylindrical shape assumed in the present researches. Based on the distinct shear stress distributions on the contact surface with the riveting die, the surface of the driven head can be partitioned on the basis of the research of E.I. Унсов (1992), which has been shown in Figure 4. The shear stress τ_c linearly increases from 0 to the maximum value in the oa range and keeps constant in the ab range. The boundary of two zones r_c approximates to the height of the formed driven head H , which is also the control factor of the automated riveting system. As the driven head height control is adopted instead of the squeezing force control in the automated riveting machine (Figure 1), a shape model of the

Figure 4 Division of the contact area of the driven head



driven head is proposed based on the height control in this section.

The shear stress on the contact surface of zone i linearly increases from 0 to $\tau_d = S/\sqrt{3}$ as:

$$\tau_c^{(i)} = \tau_d \frac{r}{H} = \frac{Sr}{\sqrt{3}H} \quad (4)$$

where S is the yield strength of rivet's material. By assuming a linear distribution through thickness, the shear stress in the driven head is given by:

$$\tau_{zr}^{(i)} = -\tau_c^{(i)} \frac{2z}{H} = -\frac{2S}{\sqrt{3}H^2} rz \quad (5)$$

According to the stress equilibrium in cylindrical coordinate system (Liu, 1994):

$$\begin{cases} \frac{\partial \sigma_r}{\partial r} + \frac{\partial \tau_{zr}}{\partial z} = 0 \\ \frac{\partial \sigma_z}{\partial z} + \frac{\partial \tau_{zr}}{\partial r} + \frac{\tau_{zr}}{r} = 0 \end{cases} \quad (6)$$

Substituting equation (5) into it, the stress equilibrium in zone i can be rewritten as:

$$\begin{cases} \frac{\partial \sigma_r^{(i)}}{\partial r} - \frac{2S}{\sqrt{3}H^2} r = 0 \\ \frac{\partial \sigma_z^{(i)}}{\partial z} - \frac{2S}{\sqrt{3}H^2} z - \frac{2S}{\sqrt{3}H^2} z = 0 \end{cases} \quad (7)$$

By solving the differential equations, the radial and squeeze stresses in the driven head of zone i can be expresses as:

$$\begin{cases} \sigma_r^{(i)} = \frac{S}{\sqrt{3}H^2} r^2 + f_1(z) \\ \sigma_z^{(i)} = \frac{2S}{\sqrt{3}H^2} z^2 + f_2(r) \end{cases} \quad (8)$$

Based on the Von Mises criterion:

$$(\sigma_r - \sigma_z)^2 + 3\tau_{zr}^2 = 0 \quad (9)$$

Substituting the stress field in zone i, the criterion can be expanded as:

$$f_1(z) - \frac{2S}{\sqrt{3}H^2} z^2 = f_2(r) - \frac{S}{\sqrt{3}H^2} r^2 + \sqrt{S^2 - \frac{4S^2 r^2 z^2}{H^4}} \quad (10)$$

A symmetrical upsetting process is assumed for the simplification of the driven head forming process, and a relative height coefficient ϕ is introduced, where $z = \phi H/2$, $\phi \in [0, 1]$, as depicted in Figure 4. Consequently, at a determined ϕ plane:

$$f_1(z) - \frac{S\phi^2}{2\sqrt{3}} = f_2(r) - \frac{Sr^2}{\sqrt{3}H^2} + \sqrt{S^2 - \frac{S^2 r^2 \phi^2}{H^2}} \quad (11)$$

To guarantee the balance of [equation \(11\)](#), whose left side has the variable z , and the right side has the variables r and z , it should equal to a constant C_1 of both sides:

$$\begin{cases} f_1(z) = C_1 + \frac{S\phi^2}{2\sqrt{3}} \\ f_2(r) = C_1 + \frac{Sr^2}{\sqrt{3}H^2} - \sqrt{S^2 - \frac{S^2r^2\phi^2}{H^2}} \end{cases} \quad (12)$$

The same manner can also be implied to zone ii. The shear stress on the contact surface keeps constant, $\tau_c^{(ii)} = S/\sqrt{3}$, and the shear stress in the driven head can be given as:

$$\tau_{sr}^{(ii)} = -\tau_c \frac{2z}{H} = -\frac{2S}{\sqrt{3}H}z \quad (13)$$

Substituting it into [equation \(6\)](#), the stress equilibrium in zone ii can be rewritten as:

$$\begin{cases} \frac{\partial \sigma_r^{(ii)}}{\partial r} - \frac{2S}{\sqrt{3}H} = 0 \\ \frac{\partial \sigma_z^{(ii)}}{\partial z} - \frac{2Sz}{\sqrt{3}Hr} = 0 \end{cases} \quad (14)$$

By solving the differential equations, the radial and squeeze stresses in the driven head of zone ii can be expresses as:

$$\begin{cases} \sigma_r^{(ii)} = \frac{2S}{\sqrt{3}H}r + g_1(z) \\ \sigma_z^{(ii)} = \frac{S}{\sqrt{3}H} \frac{z^2}{r} + g_2(r) \end{cases} \quad (15)$$

Consequently, the Von Mises criterion can be expanded as:

$$g_1(z) - \sqrt{S^2 - \frac{4S^2z^2}{H^2}} = g_2(r) + \frac{S}{\sqrt{3}H} \frac{z^2}{r} - \frac{2S}{\sqrt{3}H}r \quad (16)$$

By introducing the relative height coefficient ϕ :

$$g_1(z) - \sqrt{S^2 - S^2\phi^2} = g_2(r) + \frac{SH\phi^2}{4\sqrt{3}r} - \frac{2Sr}{\sqrt{3}H} = C_2 \quad (17)$$

Assuming that the equation above equals to a constant C_2 :

$$\begin{cases} g_1(z) = C_2 + \sqrt{S^2 - S^2\phi^2} \\ g_2(r) = C_2 + \frac{2Sr}{\sqrt{3}H} - \frac{SH\phi^2}{4\sqrt{3}r} \end{cases} \quad (18)$$

With the consideration of the boundary condition at the middle plane of $\phi = 0$:

$$\sigma_r^{(ii)} = 0, \quad \text{while} \quad r = D_m/2 \quad (19)$$

The constant C_2 can be calculated as:

$$C_2 = -\frac{SD_m}{\sqrt{3}H} - S \quad (20)$$

So, the stress field in the driven head of zone ii is given by:

$$\begin{cases} \sigma_r^{(ii)} = \frac{2S}{\sqrt{3}H}r - \frac{SD_m}{\sqrt{3}H} - S + \sqrt{S^2 - S^2\phi^2} \\ \sigma_z^{(ii)} = \frac{2S}{\sqrt{3}H}r - \frac{SD_m}{\sqrt{3}H} - S \end{cases} \quad (21)$$

Therefore, at the boundary of $r_c = H$, the radial stress can be expressed as:

$$\sigma_r^{(ii)} = \sigma_r^{(i)} = \frac{2S}{\sqrt{3}} - \frac{SD_m}{\sqrt{3}H} - S + \sqrt{S^2 - S^2\phi^2} \quad (22)$$

Combining the equation above with [equation \(12\)](#), the constant C_1 can be calculated as:

$$C_1 = \sqrt{S^2 - S^2\phi^2} - \frac{S\phi^2}{2\sqrt{3}} - \frac{SD_m}{\sqrt{3}H} - \frac{\sqrt{3}-1}{\sqrt{3}}S \quad (23)$$

and the stress field in the driven head of zone I can be given as:

$$\begin{cases} \sigma_r^{(i)} = \frac{S}{\sqrt{3}H^2}r^2 - \frac{\sqrt{3}-1}{\sqrt{3}}S - \frac{SD_m}{\sqrt{3}H} + \sqrt{S^2 - S^2\phi^2} \\ \sigma_z^{(i)} = \frac{S}{\sqrt{3}H^2}r^2 - \frac{\sqrt{3}-1}{\sqrt{3}}S - \frac{SD_m}{\sqrt{3}H} + \sqrt{S^2 - S^2\phi^2} - \sqrt{S^2 - \frac{S^2r^2\phi^2}{H^2}} \end{cases} \quad (24)$$

Consequently, the squeeze force can be formulated by integrated by squeeze stress as any determined plane ϕ with [equations \(21\)](#) and [\(24\)](#):

$$F_{sq} = \int_0^{r_c} 2\pi r \sigma_z^{(i)} dr + \int_{r_c}^{D/2} 2\pi r \sigma_z^{(ii)} dr \quad (25)$$

At the middle plane, $\phi = 0$, the squeeze force is given by:

$$F_{sq0} = 2\pi S \left\{ \begin{aligned} & \int_0^H \left[\frac{1}{\sqrt{3}H^2}r^3 - \left(\frac{\sqrt{3}-1}{\sqrt{3}} + \frac{D_m}{\sqrt{3}H} \right)r \right] dr \\ & \frac{D}{2} \int_H^{\frac{D}{2}} \left(\frac{2}{\sqrt{3}H}r^2 - \frac{D_m}{\sqrt{3}H}r - r \right) dr \end{aligned} \right. \quad (26)$$

By assuming that the squeeze force is constant through the height direction, combine [equations \(25\)](#) and [\(26\)](#), the shape of the driven head $D(\phi)$ can be formulated as:

$$\begin{aligned} & \left(\frac{D_m}{8\sqrt{3}H} + \frac{1}{8} \right) d^2 - \frac{1}{12\sqrt{3}H} d^3 - \left(\frac{D_m^3}{24\sqrt{3}H} + \frac{D_m^2}{8} \right) \\ & = \frac{H^2}{2} \sqrt{1 - \phi^2} + \frac{H^2}{3} \frac{(1 - \phi^2)^{\frac{3}{2}}}{\phi^2} - \frac{H^2}{3\phi^2} \end{aligned} \quad (27)$$

The diameter at the middle plane D_m can be evaluated using the following equation (Derijck *et al.*, 2007) with equation (26):

$$F_{sq} = \frac{\pi H_0}{4 H} D_0^2 K_r \left(\ln \frac{H_0}{H} \right)^{n_r} \quad (28)$$

where H_0 is the initial height of the driven head part, D_0 is the initial diameter of the rivet head, and K_r and n_r are the strength coefficient and the strain hardening exponent of the rivet material respectively using the power hardening rules. Afterwards, a numerical result of the shape of half of the formed driven head can be gained through equation (27).

2.1.3 Formation of the rivet shank

The volume of the deformed rivet shank can be calculated based on the volume consistency:

$$V_{Shkt} = \frac{1}{4} \pi D_0^2 (L_0 - H_C) - 2 \int_0^1 \frac{\pi}{4} D^2(\phi) d\phi \quad (29)$$

A slice model is used to analyze the stress condition of the deformed rivet shank with the assumption that the slice keeps unbending during the squeezing process, as shown in Figure 5. The circular slice suffers a different squeezing stresses $d\sigma_z$ at its both ends, while the flank sides suffer the resistant of extrusion dF_N and the friction μdF_N by the hole wall material.

The stress condition can be expressed as:

$$-\sigma_{z(r)} \pi r^2 + (\sigma_{z(r)} + d\sigma_{z(r)}) \pi (r + dr)^2 + dF_z = 0 \quad (30)$$

where dF_z is the resistant force of hole wall material along the z direction:

$$dF_z = dF_r \tan(\alpha + \rho) = |\sigma_{r(r)}| 2\pi r \tan(\alpha + \rho) dz \quad (31)$$

where $\tan \alpha = dr/dz$, and $\tan \rho = \mu$

After expanding equation (30) and neglecting high-order quantities:

$$\sigma_{z(r)} 2\pi r dr + \pi r^2 d\sigma_{z(r)} + |\sigma_{r(r)}| 2\pi r \tan(\alpha + \rho) dz = 0 \quad (32)$$

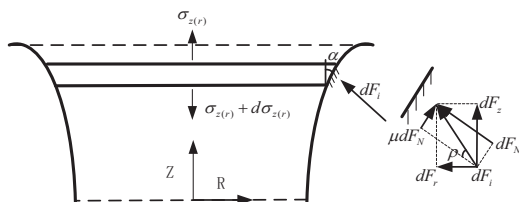
According to Tresca yield criterion:

$$|\sigma_{r(r)}| = S - \sigma_{z(r)} \quad (33)$$

Equation (32) can be sorted as:

$$\frac{d\sigma_{z(r)}}{dz} + \frac{2}{r} \sigma_{r(r)} (\tan \alpha - \tan(\alpha + \rho)) + \frac{2}{r} S \tan(\alpha + \rho) = 0 \quad (34)$$

Figure 5 Stress condition of rivet shank based on the slice model



On the other hand, the radial strain of the material of hole vicinity can be given by:

$$\varepsilon_{r(h)} = \ln \frac{r}{r_0} \quad (35)$$

The thickness variation of riveted sheets is neglected, and after the squeezing force unloaded, the sheets are approximated to be a plane stress state as (Figueira and Trabasso, 2015):

$$\varepsilon_{z(h)} \cong 0 \Rightarrow d\varepsilon_{z(h)} \cong 0, \quad \sigma_{z(h)} \cong 0 \quad (36)$$

On the basis of Levy–Mises equations, the relation of the radial and tangential stress at the hole vicinity can be obtained:

$$d\varepsilon_{z(h)} = \frac{d\varepsilon_{V(h)}}{\sigma_{V(h)}} \left[\sigma_{z(h)} - \frac{1}{2} (\sigma_{r(h)} + \sigma_{\theta(h)}) \right] = 0 \Rightarrow \sigma_{\theta(h)} = -\sigma_{r(h)} \quad (37)$$

Back into the Levy–Mises equations:

$$\begin{cases} d\varepsilon_{r(h)} = \frac{3}{2} \frac{d\varepsilon_{V(h)}}{\sigma_{V(h)}} \sigma_{r(h)} \\ d\varepsilon_{\theta(h)} = \frac{3}{2} \frac{d\varepsilon_{V(h)}}{\sigma_{V(h)}} \sigma_{r(h)} \end{cases} \quad (38)$$

and the effect strain rate at the hole vicinity can be calculated as:

$$\begin{aligned} d\varepsilon_{V(h)} &= \sqrt{\frac{2}{3} (d\varepsilon_{r(h)}^2 + \varepsilon_{\theta(h)}^2 + \varepsilon_{z(h)}^2)} = \frac{2}{\sqrt{3}} \left| d\varepsilon_{r(h)} \right| \\ \Rightarrow \varepsilon_{V(h)} &= \frac{2}{\sqrt{3}} \left| \varepsilon_{r(h)} \right| = \frac{2}{\sqrt{3}} \ln \frac{r}{r_0} \end{aligned} \quad (39)$$

Meanwhile, the effective stress at the hole vicinity is given by:

$$\begin{aligned} \sigma_{V(h)} &= \sqrt{\frac{1}{2} [(\sigma_{r(h)} - \sigma_{\theta(h)})^2 + (\sigma_{z(h)} - \sigma_{\theta(h)})^2 + (\sigma_{r(h)} - \sigma_{z(h)})^2]} \\ &= \sqrt{3} |\sigma_{r(h)}| = -\sqrt{3} \sigma_{r(h)} \end{aligned} \quad (40)$$

The radial stress in the material at the hole vicinity can be calculated by using the power law plasticity material model:

$$\begin{aligned} \sigma_{V(h)} &= K \varepsilon_{V(h)}^n \\ \Rightarrow \sigma_{r(h)} &= -\frac{1}{\sqrt{3}} K \left(\frac{2}{\sqrt{3}} \ln \frac{r}{r_0} \right)^n \end{aligned} \quad (41)$$

As at the contact interface of the rivet shank and the hole wall, the radial stresses are equal, $|\sigma_{r(r)}| = |\sigma_{r(h)}|$:

$$\sigma_{z(r)} = -S - \frac{1}{\sqrt{3}} K \left(\frac{2}{\sqrt{3}} \ln \frac{r}{r_0} \right)^n \quad (42)$$

With the assumption of exponential form, that the geometry of the deformed rivet shank can be expressed as:

$$r(z) = d(z)/2 = ae^z + b \quad (43)$$

So, the volume of the deformed rivet shank is:

$$V_{Shkt} = \int_0^{H_s} \pi r^2(z) dz = \pi \int_0^{H_s} (ae^z + b) dz \quad (44)$$

and the volume of the countersunk head is:

$$V_{Chk} = \frac{1}{3} \pi H_C \left(\frac{D_C^2}{4} + r_0^2 + \frac{D_C r_0}{2} \right) \quad (45)$$

where r_0 is the radius at the interface of the deformed rivet shank and the countersunk head.

Substituting equation (42) into equation (34):

$$2\mu \left[S + \frac{1}{\sqrt{3}} K \left(\frac{2}{\sqrt{3}} \ln \frac{ae^z + b}{r_0} \right)^n \right] - \frac{2nKa e^z}{3} \left(\frac{2}{\sqrt{3}} \ln \frac{ae^z + b}{r_0} \right)^{n-1} + 2S(ae^z + \mu) = 0 \quad (46)$$

By the combination of equation (46) and the volume consistency of equations (3), (44) and (45), the geometry parameter of the rivet shank, a and b , can be obtained.

2.2 Prediction of the dimensional accuracy using rivet equivalent unit

2.2.1 Principle of the numerical approach for the dimensional accuracy prediction

As the aircraft components are usually large-scaled with many rivets inserted, the detailed non-linear FE method for the simulation of the global deformation is inappropriate, or even impossible. To reduce the complexity of the problem and get an industrial relevant solving time, alternative methods are usually employed to approximate the compressive stresses on the local joints by applying the same distortion effects to the adjacent material around the hole.

A common modeling technique is the sub-modeling approach, which represents part of a structure as any equivalent load or component that can apply the correct forces and moments to the sheets at the inner surface of the rivet hole. In this study, the local material with a non-uniform compressive stress field around the hole is partitioned from the whole model and divided into two layers of same sizes with an assignment of different thermal expansion coefficients, while the rest of the part is assigned with no thermal material properties. The radius of the local unit is suggested larger than the elastic-plastic boundary at the hole vicinity, and by using the temperature changes the radial expansion in the elastic region can be simulated. That is, the expansion coefficients of the equivalent component is represented by the thermal expansion coefficient α_1 and α_2 , while the elastic deformation is accomplished by the temperature change Δt . Moreover, the change of the joint stiffness due to the insertion of rivets is neglected in this study, and the equivalent joint effect is implemented through the beam rigid connection with Multi-Points Constrains (MPC). The equivalent rivet unit is shown in

Figure 6 The simplified model for local joint

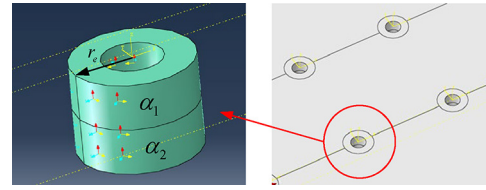


Figure 6. Afterwards, the equivalent units are applied at each location of riveting hole. By specifying a uniform temperature filed change in the finite element model, the two layers will expand in different extents and result in an approximation of both forces and moments applied onto the outer and inner sheets respectively. The result would be a net expansion in the plane and a deflection transverse. In this study, all the local units are constructed in the global-level at once, and the riveting sequence is neglected.

2.2.2 Determination of the parameters of rivet equivalent unit

To simplify the modeling process, the temperature change Δt in the model is chosen to be unit. Consequently, the value of the expansion coefficients α_1 and α_2 can be determined directly on the basis of the local distortions. Due to the through-thickness variation of interference, the average expansions are obtained through integral along the radial direction at a specific radius r_e for both the outer and inner sheets.

The core of constructing the equivalent model is the determination of the relationship between the distance r and its corresponding strain field $\varepsilon_{r(h)}$. There are two distortion regions in the sheet material at hole vicinity. The plastic region extends from the hole wall $r(z)$ to the boundary indicated by r_{db} and the elastic region starts from this specific point. At the boundary r_{db} the effective stress in the sheet should equal to the yield strength:

$$\sigma_{V(h)} = S_{(h)} \quad (47)$$

According to equation (37), the stress equilibrium of the sheet material can be given by:

$$\frac{\sigma_{r(h)}}{dr} + \frac{2}{r} \sigma_{r(h)} = 0 \quad (48)$$

Its solutions have the following form as:

$$\sigma_{r(h)} = \frac{C_3}{r^2} \quad (49)$$

Considering that equation (41) exists at the hole wall, the coefficient C_3 is obtained as:

$$C_3 = -\frac{R^2}{\sqrt{3}} K \left(\frac{2}{\sqrt{3}} \ln \frac{R}{r_0} \right)^n \quad (50)$$

Therefore, the boundary of the elastic and plastic regions can be calculated as:

$$r_d = \sqrt{\frac{C_3}{S_{(h)}}} = \sqrt{\frac{R}{S_{(h)}} K \left(\frac{2}{\sqrt{3}} \ln \frac{R}{r_0} \right)^n} \quad (51)$$

Afterwards, based on the Hook's law, while $r > r_d$, there is:

$$\varepsilon_{r(h)} = \frac{1}{E} [\sigma_{r(h)} - \nu(\sigma_{\theta(h)} + \sigma_{z(h)})] = \frac{1+\nu}{E} \sigma_{r(h)} \quad (52)$$

With the consideration of equations (40) and (47), at the boundary r_d :

$$\sigma_{r(h)} = -\frac{1}{\sqrt{3}} S_{(h)} = \frac{C_3}{r_d^2} \Rightarrow C_3 = -\frac{r_d^2}{\sqrt{3}} S_{(h)} \quad (53)$$

So, the radius strain of sheet material in the elastic region can be expressed as:

$$\varepsilon_{r(h)} = -\frac{(1+\nu)S_{(h)}}{\sqrt{3}E} \left(\frac{r_d}{r}\right)^2 \quad (54)$$

Afterwards, the expansion coefficients α_1 and α_2 of the equivalent unit can be determined through integral along the radial expansion with specific radius r . The radial expansion can be calculated as:

$$u_{r(h)} = \int \varepsilon_{r(h)} dr = \int \left[-\frac{(1+\nu)S_{(h)}}{\sqrt{3}E} \left(\frac{r_d}{r}\right)^2 \right] dr \quad (55)$$

Since the thermal expansion of the equivalent model is constrained by the rest material of the plates, the stress equilibrium due to the radial expansion can be given based on the Hook's law:

$$\sigma_{re} = \frac{E}{1+\nu} (\varepsilon_{re} - \varepsilon_{th}) = \sigma_{rr} = -\frac{E}{1+\nu} \varepsilon_{re} \Rightarrow \varepsilon_{th} = 2\varepsilon_{re} \quad (56)$$

where ε_{re} is the total strain and ε_{th} is the thermal strain. Consequently, the expansion coefficients α_1 and α_2 are determined by dividing the corresponding average radial expansion of the outer and inner sheets by the specified radius r_e :

$$\alpha_1 = \bar{u}_{r1(h)}/4(r_e - r_0), \quad \alpha_2 = \bar{u}_{r2(h)}/4(r_e - r_0) \quad (57)$$

3. Experimental test for single and multiple countersunk riveting

In this section, experiments of both the single and multiple countersunk riveting process are designed and fully carried out for the validation of the proposed methods in Section 2. The numerical results and experimental measurements regarding

the counter of single riveting are compared to the analytical result for the local distortion analysis. Afterwards, test specimens with multiple riveting are designed and riveted sequentially before growth measurements are commenced using a co-ordinate measuring machine.

3.1 Tests on single riveting

3.1.1 Geometric information and material properties

There are two kinds of rivets with different radii used in the experimental tests for single riveting. The geometry information of the rivets is depicted in Figure 7. Both of them have the 100° countersunk heads.

Single rivets are squeezed in double-layered sheet metals. The material of 4 mm rivet is Al2117-T4 with corresponding to the sheet metal of Al2024-T3, while the material of 5 mm rivet is 7075-T3 with corresponding to the sheet metal of Al7075-T7451. The material properties are listed in Table II. An isotropic hardening behavior is assumed to for both two pairs of material. The strength coefficients K and hardening coefficients n can be determined based on the test data of the true stress and strain for each material. By transformed the power hardening expression into the logarithm naturel-based format:

$$\sigma = K(\varepsilon)^n \Rightarrow \ln \sigma = \ln K + n \ln \varepsilon \quad (58)$$

The linear fitting is applied to fit the curve data of the test data between $\ln \sigma$ and $\ln \varepsilon$, as the hardening coefficient n is the slope of the fitted line, and the true stress where the strain $\varepsilon = 1.0$ is the strength coefficient K . Afterwards, these hardening coefficients will be applied into equations (28) and (46) of the analytical model proposed in Section 2.1.

Figure 7 Geometry of 4 mm (a) and 5 mm (b) rivets

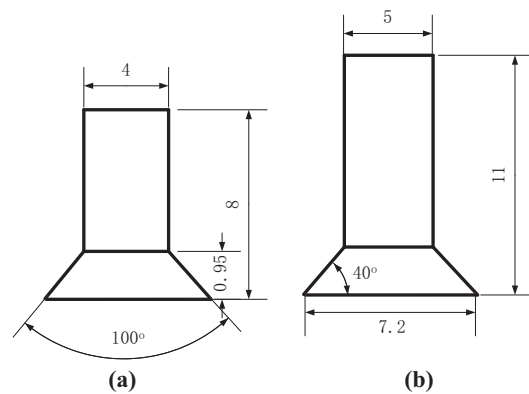


Table II Summary of the material properties used for both rivets and sheet metals

	Rivet (2117-T4)	Sheets (2024-T3)	Rivet (7050-T73)	Sheets (7050-T7451)
Young's modulus	71.700 GPa	72.4 GPa	72 GPa	71.7 GPa
Poisson ratio	0.33	0.33	0.33	0.33
Yield strength	311.3 MPa	345 MPa	435 MPa	469 MPa
Strength coefficient	551 MPa	730 MPa	350 MPa	350 MPa
Hardening coefficient	0.15	0.157	0.3	0.3

3.1.2 Simulation and experimental results

The detailed nonlinear FE models of single riveting are generated through the commercial FE software ABAQUS 6.10, as shown in Figure 8. Power law plasticity models is used to describe the non-linear material behavior, and contact is implemented to the interfaces between sheets and rivets. As the lower riveting head is planar, a rigid plane is modeled as the riveting punch to apply the squeeze forces to the tail of rivet shank, and the height control of driven head is transformed into the displacement boundary condition applied to the rigid tool. In the FE models, single rivets are squeezed in the center of 100 mm × 100 mm square double-layered specimens, which is supposed to be large enough for a negligible effect of the stress free outer boundaries. Boundary conditions are applied in the relative three directions. The total thickness of the specimens for 4 mm holes is 2.9 mm, with a 1.6 mm inner sheet and a 1.3 mm outer sheet, while the total thickness of 5 mm holes is 4.8 mm with both 2.4 mm sheets. The clearance between the rivet and hole, which is collected from the following experimental specimens, are 0.064 mm for 4 mm rivet and 0.051 mm for 5 mm rivet. The FE models are calculated through the Abaqus/Explicit.

Experiments on large specimens with the same thickness configuration are carried out on the independently developed automated riveting machine in Figure 1. The rivet pitch is controlled over 5 times the radii of the corresponding rivets to prevent them from interfering with each other. The controlled height of the driven head is 2.24 mm for 4 mm rivets, and 2.53 mm for 5 mm rivets. Afterwards, three rivets for each diameter are selected and extracted from the specimens. The measurements of the cross section are taken on the XT digital internal micrometer to obtain the dimensions of the rivets at its plane of symmetry as suggested by Szolwinski and Farris (2000).

The numerical and experimental results are compared to the analytical model. As shown Figure 9, a photograph of a sectioned riveted joint of 4 mm with an overlay of a corresponding deformed finite element mesh is presented. The comparisons of measured, numerical and the analytical values for several geometric characteristics of the installed rivet configurations are listed in Table III. The parameters of shape function of the rivet shank is $a = 1.124\text{E-}3$ and $b = 2.066$ for 4 mm rivet, and $a = 9.40\text{E-}4$ and $b = 2.577$ for 5 mm rivet, respectively.

The comparisons of the counters of the driven head and the rivet shank are shown in Figures 10 and 11. From the results,

Figure 8 Detailed nonlinear FE model of single rivet

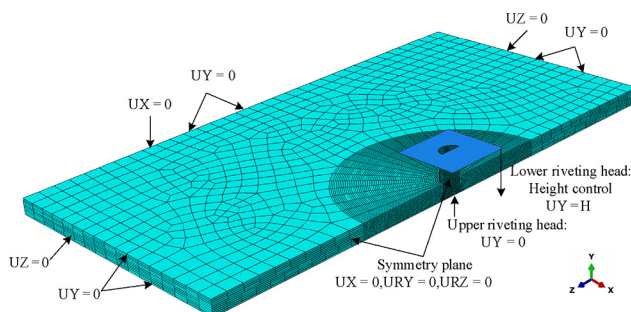
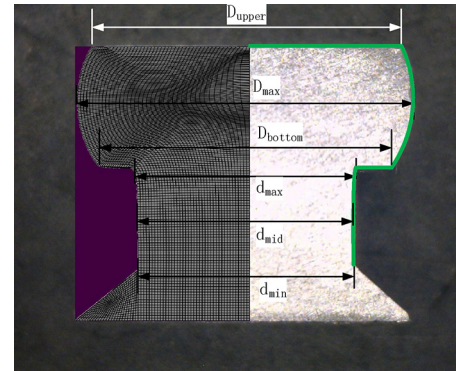


Figure 9 A polished cross section with an overlay of corresponding deformed finite element meshes



we can see a more precise contour of the deformed rivets is able to be achieved with the consideration of the barrel-like driven head and the through-thickness variations along the rivet shank than the traditional assumption of cylindrical deformations when compared to the measurement data. The average deviation of the driven head is about 3.54 per cent comparing with the experiment results and 0.68 per cent comparing with the FE simulations. The maximum deviations occur at the upper surface of the driven head, approximating 7 per cent while comparing to the measurement data. This is mainly caused as the real formed driven head is not symmetric in the middle plane due to the different stress conditions of both ends, while in the analytical study, an independent upsetting is assumed. The maximum diameter of the real driven head usually deviates to the side of the contact surface with the riveting punch. The deformations of the 4 mm rivet shank tend to be more uniform through thickness, while the counter of the deformed 5 mm rivet shank is more approximated to the assumption of exponential form. This may be attributed to the increasing thickness of the test specimens from 2.9 mm of 4 mm rivet to 4.8 mm of 5 mm rivet.

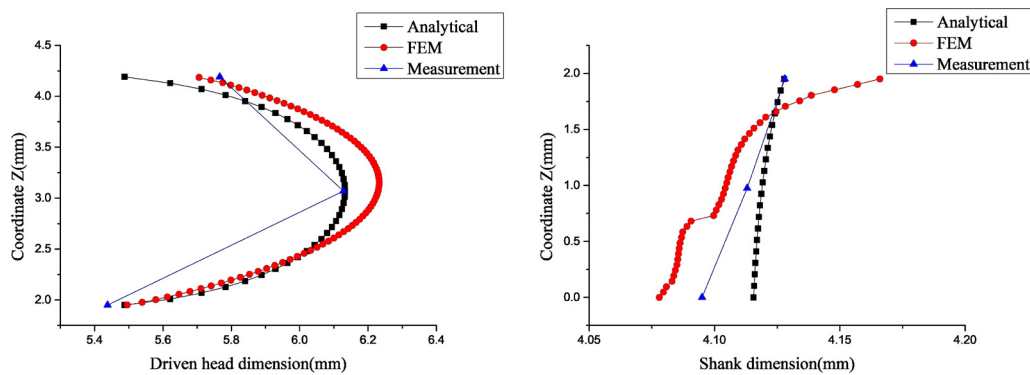
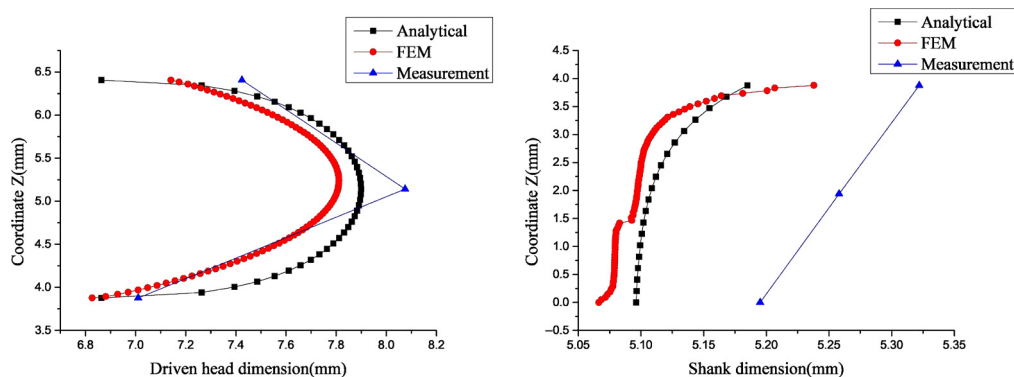
3.2 Tests on multiple riveting specimen

3.2.1 Sheet metal specimens and experiment design

The validation of the global deformation prediction is carried out in this section. The local equivalent rivet units proposed in Section 2.2 are applied to a series of small panel assemblies, and compared with the experimental measurements. These panel assemblies are all double-layered laminated sheets, and is designed and manufactured with various dimensions. There two different sizes for the 4 mm riveting specimens. The small specimens are 400 mm long and 40 mm wide with a 1.6 mm thickness inner sheet and a 1.3 mm outer sheet. 12 riveting holes are arranged on the centerline of the specimens with 30 mm rivet pitches. The larger specimens are 630 mm long and 130 mm wide with both 2.4 mm thickness sheets. Three rows of total 48 riveting holes are arranged on the specimens with 28 mm rivet pitches. The material of the rivets and sheets are Al2117-T4 and Al2024-T3 respectively. The riveting specimens are 270 mm long and 30 mm wide with both 2.4 mm thickness sheets. Eleven riveting holes are arranged on the centerline of the specimens with 25 mm rivet pitches. The dimensions of all three specimens are shown in Figure 12.

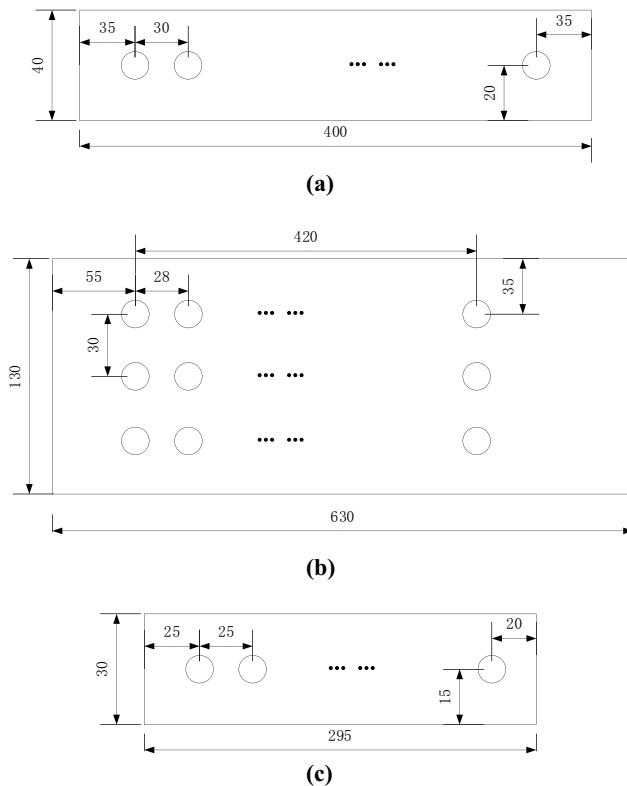
Table III Comparisons of measured, numerical and analytical values for various geometric characteristics of installed rivets (unit: mm)

	Driven head				Rivet shank			
	Max. D	Up. D	Bot. D	Mean D	Max. d	Mid. D	Min. d	Mean d
4 mm								
Analytical	6.133	5.488	5.488	5.959	4.128	4.119	4.116	4.120
FEM	6.232	5.706	5.495	6.019	4.166	4.104	4.078	4.105
Deviation	1.59%	3.83%	0.13%	1.00%	0.91%	0.37%	0.93%	0.37%
Experimental	6.194	5.832	5.590	—	4.144	4.121	4.108	4.124
Deviation	0.99%	5.91%	1.83%	—	0.39%	0.05%	0.19%	0.11%
5 mm								
Analytical	7.900	6.864	6.864	7.686	5.185	5.112	5.096	5.102
FEM	7.811	7.141	6.827	7.527	5.238	5.097	5.066	5.108
Deviation	1.14%	3.88%	0.54%	2.11%	1.01%	0.29%	0.59%	0.12%
Experimental	8.075	7.424	7.010	—	5.322	5.258	5.195	5.258
Deviation	2.22%	8.16%	2.13%	—	2.57%	2.78%	1.91%	2.97%

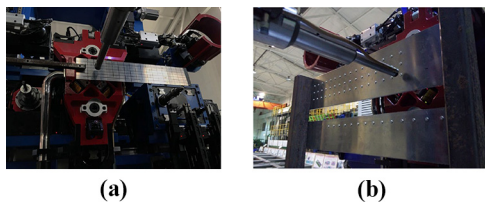
Figure 10 Comparison of 4 mm countersunk rivet counter**Figure 11** Comparison of 5 mm countersunk rivet counter

The specimens are clamped on a dedicated fixture as shown in Figure 13. The fixture is designed to release the riveting deformations along the specimens' longitude directions, excluding the influence of boundary conditions on the panel deformations. The 4 mm small specimens and the 5 mm specimens are fastened to the fixture at the left short edge with one pre-drilled location hole, while the 4 mm large specimens are fixed at the left edge with two pre-drilled locations holes. For all three specimens, small

pressure is applied to the opposite side of the fixed edges to prevent the deformations caused by their self-weight and allow them to expand under the resistant friction force. The riveting processes are programmed and conducted on the automated riveting machine based on the designed riveting locations. For accumulating the distortions in the same direction, the riveting sequence starts from the clamped side to the free edge side. The large specimens with three rows of rivets use a "N" pattern path to

Figure 12 Multiple riveting specimens

Note: (a) 4 mm small specimen; (b) 4 mm large specimen; (c) 5 mm specimen

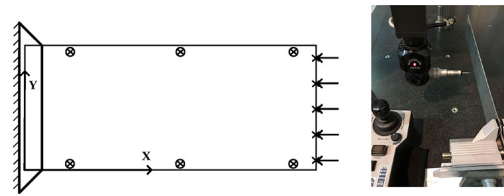
Figure 13 Multiple riveting tests on dedicated fixture

accomplish each column first. The controlled height of the driven head is 2.25 mm for 4 mm rivets, and 2.2 mm for 5 mm rivets, respectively.

The dimension of the specimens before and after riveting is measured by using the three coordinate measuring machine. The dimension growth can be obtained by comparing the two sets of data, excluding the influence of the manufacturing error of the specimens. As shown in Figure 14, on the three coordinate measuring machine, the clamped edges on the dedicated fixture is also positioned vertically as the Y datum, and 5 measuring points is uniformly distributed on the opposite free edges. There are six holes distributed along the X direction on the longitude edge, which are used to evaluate the positioning deviation of the specimens before and after riveting process.

3.2.2 Equivalent model and FE simulations

Since the small panel assemblies are designed with the same double-layered configuration in tests on single riveting, the results

Figure 14 Measurement on the coordinate measuring machine

of local distortions acquired before can be directly adopted to develop the equivalent model. The resultant expansion coefficients α_1 and α_2 for inner and outer sheets with the corresponding unit radius r are calculated as the method proposed in Section 2.2. The local riveting units are constructed accordingly and imbedded into the global model of each specimen in ABAQUS as shown in Figure 6. The boundary conditions are applied to the panel assemblies at the corresponding directions to simulate the constraints of the specimens on the dedicated fixture during riveting. Afterwards, a uniform temperature filed change is applied to the model, and the two layers of equivalent models will expand in different extents and simulate the net expansion and deflection transverse in the small panel assemblies. Take the 4 mm large specimens as an example, the FE model is constructed and shown in Figure 15. The FE model is meshed with C3D8R, and contains 73107 elements. The fixed boundary conditions are applied to the left edge of the specimen to simulate the clamping conditions on the dedicated fixture. In total, 48 equivalent rivet units are distributed at the corresponding riveting hole position. By increasing 1 degrees in the first analysis step, the local deformation is simulated by the thermal expansion effect of the equivalent unit, and the global distortions can be obtained consequently.

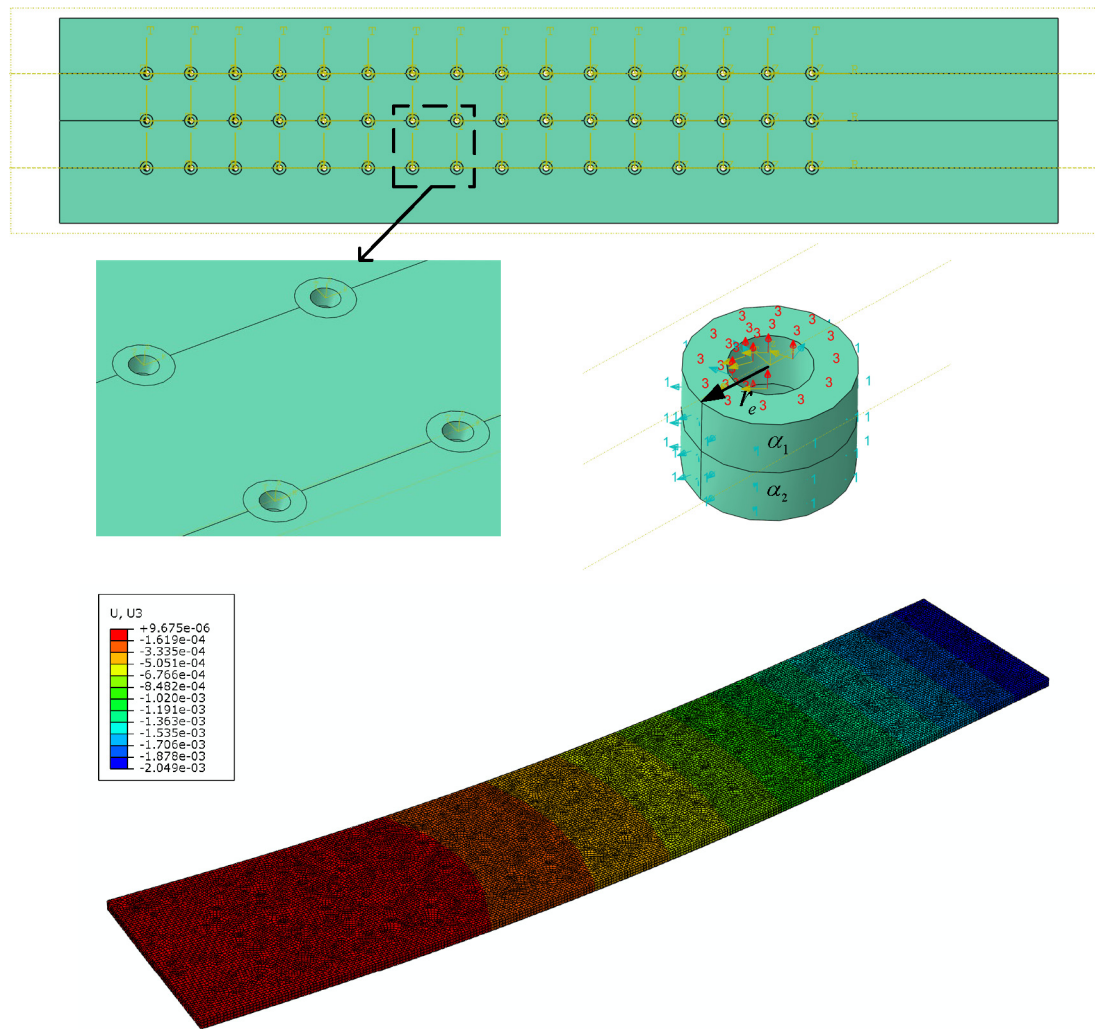
3.2.3 Simulation and experiment results

A total of 20 small panel assemblies are manufactured and tested, ten samples of small specimens and five samples of large specimens for 4 mm rivets and five samples of specimens for 5 mm rivets. The mean growth of the panel assemblies is listed in Table IV.

From the results, we can see that the proposed local riveting unit for the global distortion of panel assemblies has acceptable accuracy when compared to the measurement data. The average deviation of the expansion in-plane is 31.9 per cent, while the average deviation of the deflection out-of-plane is 5.19 per cent. Considering that the extent of the linear expansion is small in this configuration of tested panel assemblies, the deviations of the linear expansions can be acceptable. The results also show that, comprising to the magnitude of linear expansion, the deflection out-of-plane caused by the accumulation of through-thickness variations is more significant for the riveted specimens. It confirms that the consideration of this through-thickness variations is essential while analyzing the growth of riveted panel assemblies. Furthermore, with the comparison of the results from 4 mm small specimens and 5 mm specimens, the larger interferences of local joints cause more dimensional growth of the riveted panel though their thickness is different.

4. Conclusion

In the automated riveting process of the aircraft panel assembly, an effective calculation method for the rivet-induced dimensional error is required to support the error reduction of assemblies with

Figure 15 Simulation results of 4 mm large specimen**Table IV** The measurements and simulation results of multiple riveting tests (mm)

Cat	Expansion in-plane			Deflection out-of-plane		
	Meas	Simu	Diff (%)	Meas	Simu	Diff (%)
4 mm Small	0.032	0.045	40.6	1.890	2.012	6.46
4 mm Large	0.083	0.061	26.5	2.220	2.049	7.70
5 mm	0.063	0.081	28.6	2.421	2.388	1.36

many rivets. This paper presents a local-global method for predicting the deformations of the riveted panel assembly. A simplified analytical study is performed to analyze the deformations of single rivets with the consideration of the barrel-like shape of the driven head and the through-thickness variations along the rivet shank. Afterwards, the displacement field around the connection area have been calculated for the development of a local equivalent unit. The simplified model is modeled with temperature and thermal expansion coefficients with corresponding unit radius r_e and embedded into the global-level

model for the prediction of the overall distortions of riveted sheets. Finally, experimental tests are designed and carried out for the validation of the proposed method on an automatic riveting machine developed independently. The results indicated that the analytical study is able to reach a more precise contour of the deformed rivet than the traditional assumption of cylindrical deformations, and rapidly determine the equivalent coefficients of the local riveting unit. The comparison with experimental tests shows an industrial acceptable accuracy of the prediction model for the global distortions of the double-layered test specimens, whose configuration is widely used in the aircraft panel assembly. By programming the calculation process of the local equivalent unit through MATLAB and integrating it into the code developed by python language in ABAQUS, the proposed method can be applied to the riveting section allocation and riveting sequence optimization for large-scaled panel assembly. However, in this study, the initial state of riveting panel sheets are assumed in the ideal conditions with stress free boundary. The influence of the previous pre-joining step before the automated riveting process is not included. Further investigation should aim at the change of the local distortion pattern with clearance distributions and the

mapping results of panel sheets under discrete constraints of pre-joining joints.

References

- Abdelal, G.F., Georgiou, G., Cooper, J., Robotham, A., Levers, A. and Lunt, P. (2015), "Numerical and experimental investigation of aircraft panel deformations during riveting process", *Journal of Manufacturing Science and Engineering*, Vol. 137 No. 1, p. 011009.
- Aman, F., Cheraghi, S.H., Krishnan, K.K. and Lankarani, H. (2013), "Study of the impact of riveting sequence, rivet pitch, and gap between sheets on the quality of riveted lap joints using finite element method", *The International Journal of Advanced Manufacturing Technology*, Vol. 67 Nos 1/4, pp. 545–562.
- Blanchot, V. and Daidie, A. (2006), "Riveted assembly modelling: study and numerical characterisation of a riveting process", *Journal of Materials Processing Technology*, Vol. 180 Nos 1/3, pp. 201–209.
- Chang, Z., Wang, Z., Jiang, B., Zhang, J., Guo, F. and Kang, Y. (2016), "Modeling and predicting of aeronautical thin-walled sheet metal parts riveting deformation", *Assembly Automation*, Vol. 36 No. 3, pp. 295–307.
- Cheng, H., Li, Y., Zhang, K., Mu, W. and Liu, B. (2011), "Variation modeling of aeronautical thin-walled structures with multi-state riveting", *Journal of Manufacturing Systems*, Vol. 30 No. 2, pp. 101–115.
- Cheng, H., Wang, R.X., Li, Y. and Zhang, K.F. (2012), "Modeling and analyzing of variation propagation in aeronautical thin-walled structures automated riveting", *Assembly Automation*, Vol. 32 No. 1, pp. 25–37.
- Cheraghi, S.H. (2008), "Effect of variations in the riveting process on the quality of riveted joints", *The International Journal of Advanced Manufacturing Technology*, Vol. 39 Nos 11/12, pp. 1144–1155.
- DeRijck, J., Homan, J., Schijve, J. and Benedictus, R. (2007), "The driven rivet head dimensions as an indication of the fatigue performance of aircraft lap joints", *International Journal of Fatigue*, Vol. 29 No. 12, pp. 2208–2218.
- Eckert, A., Israel, M., Neugebauer, R., Rossinger, M., Wahl, M. and Schulz, F. (2013), "Local-global approach using experimental and/or simulated data to predict distortion caused by mechanical joining technologies", *Production Engineering*, Vol. 7 Nos 2/3, pp. 339–349.
- УНКОВ, Е.И. (1992), *Theory of Metal Plastic Forming (in Chinese)*, Machinery Industry Press, (translated by ZR Wang).
- Figueira, J.A.N. and Trabasso, L.G. (2015), "Riveting-Induced deformations on aircraft structures", *Journal of Aircraft*, Vol. 52 No. 6, pp. 2032–2050.
- Kaniowski, J., Wronicz, W., Jachimowicz, J. and Szymczyk, E. (2009), "Methods for FEM analysis of riveted joints of thin-walled aircraft structures within the IMPERJA project", *25th ICAF Symposium, Bridging the Gap between Theory and Operational Practice in Rotterdam*, Springer, Dordrecht, pp. 939–967.
- Langrand, B., Patronelli, L., Deletombe, E., Markiewicz, E. and Drazetic, P. (2002a), "Full scale experimental characterisation for riveted joint design", *Aerospace Science and Technology*, Vol. 6 No. 5, pp. 333–342.
- Langrand, B., Patronelli, L., Deletombe, E., Markiewicz, E. and Drazetic, P. (2002b), "An alternative numerical approach for full scale characterisation for riveted joint design", *Aerospace Science and Technology*, Vol. 6 No. 5, pp. 343–354.
- Li, G., Shi, G. and Bellinger, N.C. (2006a), "Studies of residual stress in single-row countersunk riveted lap joints", *Journal of Aircraft*, Vol. 43 No. 3, pp. 592–599.
- Li, G., Shi, G. and Bellinger, N.C. (2006b), "Study of the residual strain in lap joints", *Journal of Aircraft*, Vol. 43 No. 4, pp. 1145–1151.
- Lin, J., Jin, S., Zheng, C., Li, Z. and Liu, Y. (2014), "Compliant assembly variation analysis of aeronautical panels using unified substructures with consideration of identical parts", *Computer-Aided Design*, Vol. 57 29/5740.
- Liu, G., Huan, H. and Ke, Y. (2014a), "Study on analysis and prediction of riveting assembly variation of aircraft fuselage panel", *The International Journal of Advanced Manufacturing Technology*, Vol. 75 Nos 5/8, pp. 991–1003.
- Liu, G., Tang, W., Ke, Y., Chen, Q. and Bi, Y. (2014b), "Modeling of fast pre-joining processes optimization for skin-stringer panels", *Assembly Automation*, Vol. 34 No. 4, pp. 323–332.
- Liu, W. (1994), "Shape solution after cylinder upsetting between rough planes using equilibrium differential equation (in Chinese)", *Metal Forming Technology*, Vol. 12 No. 1, pp. 37–41.
- Manes, A., Giglio, M. and Viganò, F. (2011), "Effect of riveting process parameters on the local stress field of a T-joint", *International Journal of Mechanical Sciences*, Vol. 53 No. 12, pp. 1039–1049.
- Munk, C.L., Nelson, P.E. and David, E.S. (2004), Determinant Wing Assembly, US Patent No. 6,808,143, 26 October.
- Ni, J., Tang, W., Xing, Y., Beb, K. and Li, M. (2016), "A local-to-global dimensional error calculation framework for the riveted assembly using finite-element analysis", *Journal of Manufacturing Science and Engineering*, Vol. 138 No. 3, p. 031004.
- Saadat, M. and Cretin, C. (2002), "Dimensional variations during airbus wing assembly", *Assembly Automation*, Vol. 22 No. 3, pp. 270–276.
- Saadat, M., Sim, R. and Najafi, F. (2007), "Prediction of geometrical variations in Airbus Wingbox assembly", *Assembly Automation*, Vol. 27 No. 4, pp. 324–332.
- Szolwinski, M.P. and Farris, T.N. (2000), "Linking riveting process parameters to the fatigue performance of riveted aircraft structures", *Journal of Aircraft*, Vol. 37 No. 1, pp. 130–137.
- Wang, H. (2014), "Riveting sequence study of horizontal stabilizer assembly using finite-element analysis and riveting equivalent unit", *Journal of Aerospace Engineering*, Vol. 27 No. 6, pp. 04014040.

Corresponding author

Weiwei Qu can be contacted at: qwwwwl@zju.edu.cn